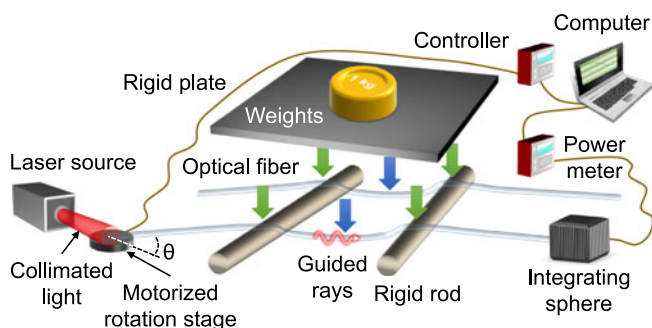# Force Sensors Using the Skew-Ray-Probed Plastic Optical Fibers

George Y. Chen
Soroush Shahnia
Tanya M. Monro
David G. Lancaster

Force Sensors Using the Skew-Ray-Probed Plastic Optical Fibers

George Y. Chen [iD] **, Soroush Shahnia** [iD] **, Tanya M. Monro** [iD] **,
and David G. Lancaster** [iD]

Laser Physics and Photonic Devices Laboratories, School of Engineering, University of
South Australia, Mawson Lakes, SA 5095, Australia

Abstract: Simple optical force sensors have many uses but suffer from relatively low sensitivity or low fabrication-tolerance. We have demonstrated that pure skew rays can enhance the sensitivity of a bend-loss-based force sensor over the mixture of rays created from a normal incidence by a factor of 3.8 to enable a sensitivity of 0.126 dB/N. The dynamic range was measured from 222.2 mN to >14.1 N. The response/recovery times were found to be 500 and 600 ms, respectively. We also showed a compression-loss-based force sensor exhibiting a small deviation of 6.7% in sensitivity of 0.015 dB/N against the changes in the launch angle of light. The dynamic range was tested from 875.0 mN to >24.2 N. The response/recovery times were observed as 350 and 300 ms, respectively. The sensitivity of these force sensors can be further enhanced with geometry and fiber-material changes, and the enhancement technique could be extended to other designs.

Index Terms: Force sensor, plastic optical fiber, skew rays.

1. Introduction

Force sensors provide a measure of weights and physical impact across a wide array of applications in industries such as construction, manufacturing, automotive, mining, storage, biomechanics, sports, instruments and devices [1]. The problems with most simple force sensors are their relatively low sensitivity, low fabrication-tolerance and vulnerability to electromagnetic interference (EMI), which prevents them from being deployed in a diverse range of environments. Overcoming these hurdles can benefit the aforementioned industries, allowing more aspects of our modern world to be smart and safely controlled. Optical force sensors are advantageous in that their dielectric construction renders them immune to EMI [2]. Many practical designs have been reported, employing straight step-index fibers [3], straight graded-index fiber [4], fiber Bragg gratings [5]–[7], coiled fiber [8], bent fiber [9], bifurcated fiber [10], polarimetric birefringent fiber [11], optical microfiber Fabry Perot [12], cross fibers [13] and distributed Bragg reflector (DBR) fiber laser [14]. A number of these designs are based on plastic optical fibers (POFs), due to their relatively low cost and flexibility which leads to a higher sensitivity and a wider dynamic-range [15]. The straight-fiber design is the simplest, though it requires more advanced materials for its detection limit (e.g., 50 mN [3]) to be competitive with more sophisticated designs using more basic materials (49 mN [9]). Although the DBR-based design has some of the lowest detection limits (755 μN), the fabrication and
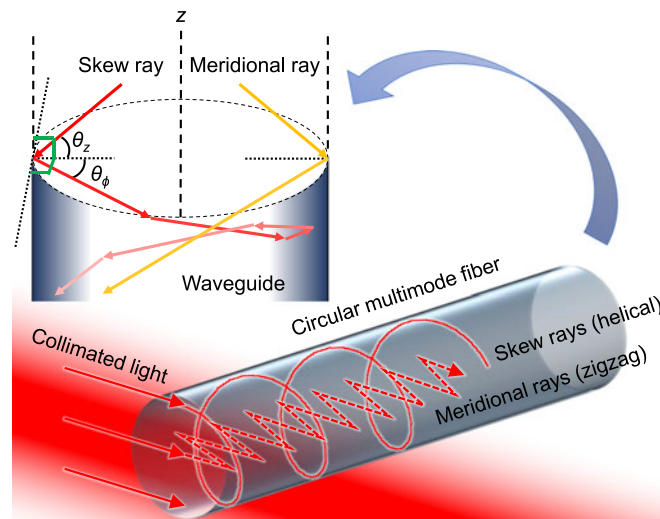
Fig. 1. Illustration of skew rays propagating with longitudinal and transverse angles, thus providing coverage of the fiber interface.

experimental setup are considerably more complex and expensive. Depending on the requirement for detection limit and cost, end users have a spectrum of fiber-optic force sensors to choose from.

To enhance the sensitivity and improve the fabrication tolerance of the straight-fiber design, such that it can compete with more sophisticated designs, we present the skew-rays enhancement technique on force sensors for the first time. As examples, we present two new designs of POF-based force sensors which respond to downward forces, and thus are suitable for applications such as weight sensors for light vehicles on roads, and platforms in power stations.

2. Principles

Skew rays [16]–[18], or vortex modes with possible orbital angular momentum [19], evolve from meridional rays at the curved interface of a cylindrical multimode fiber, as illustrated in Fig. 1. They propagate in a helical pattern that never crosses the fiber axis.

Firstly and secondly, skew rays yield more total internal reflections and total cladding-penetration path length per unit length than meridional rays. Thirdly, they provide a more complete coverage along the circular cladding-coating interface, which enable the optical fiber to sense forces from all directions. Lastly, they can also utilize the cut-off effect beginning with meridional rays and low-order skew rays. The first three factors increase the chances of rays encountering localized physical perturbations that attenuate light. Thus, render skew rays are much more sensitive than meridional rays per unit fiber length, and are used for a variety of sensing applications [20]–[23] such as fiber defect detection [22]. The first (i.e., dominant), third and fourth factors are relevant to the proposed force sensors. A more accurate number of reflections per unit fiber length (N_r) is reported for the first time [i.e., left side of Eq. (1)], which can be derived from [17]. In the literature, the error in N_r caused by neglecting d [right side of Eq. (1)] can be as high as -30%.

$$N_r = 1 / \left(\left[\frac{2R \cos \theta_\phi}{\cos \theta_z} + d \right] \cdot \sin \theta_z \right) \approx \frac{\cot \theta_z}{2R \cos \theta_\phi} \tag{1}$$

where θ_z and θ_ϕ are the angle between the rays and the normal to the core-cladding interface seen from the transverse and longitudinal perspectives respectively, R is the cladding radius, and d is the Goos-Hänchen shift.

As the launch angle (θ) increases from zero, the rays inside an optical fiber evolve from a mixture of low-order meridional rays (i.e., high θ_z) and low-order skew rays (i.e., low θ_ϕ), to a mixture of
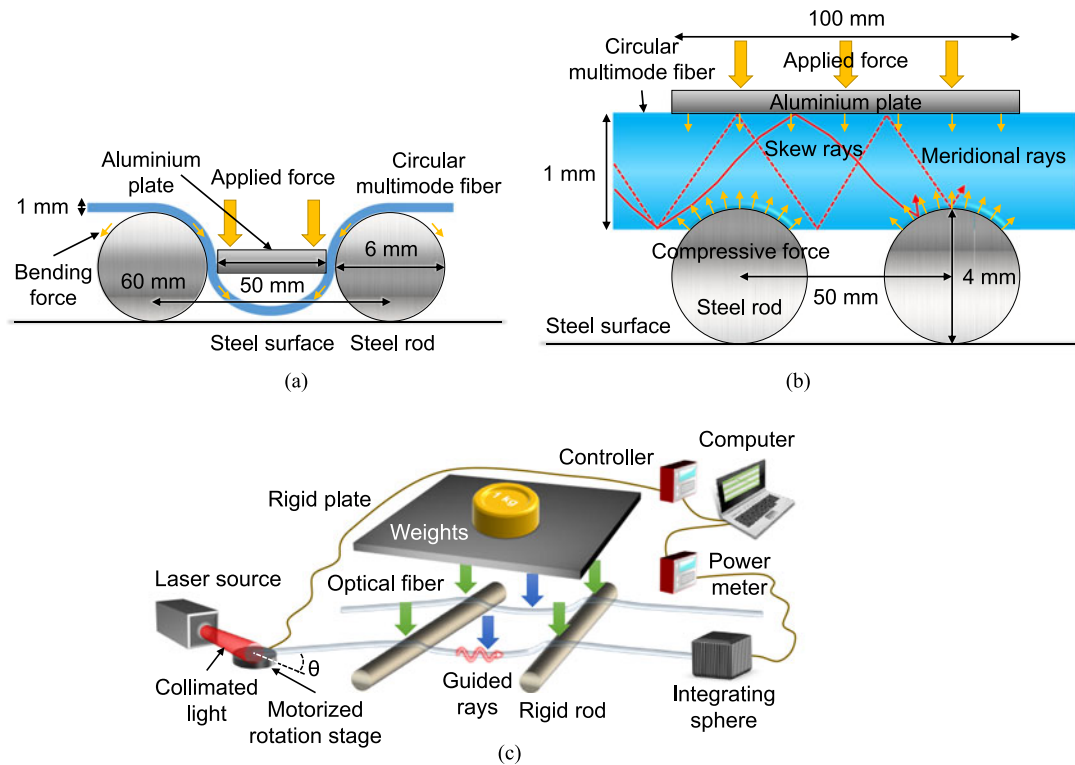
Fig. 2. (a) First force sensor: schematic of the sensing fiber. (b) Second force sensor: schematic of the sensing fiber. (c) Schematic of the experimental setup for both force sensors. All schematics are not drawn to scale. Blue arrows indicate the applied force for the first force sensor, while green arrows are associated with the second force sensor, not drawn to scale.

high-order meridional rays (i.e., low θ_z) and medium-order skew rays (i.e., medium θ_ϕ). Beyond the acceptance angle, all meridional rays leak out and the rays comprise only high-order skew rays (i.e., high θ_ϕ). Although θ_z and θ_ϕ have no direct relationship, the former can be manipulated through θ to filter the range of θ_ϕ.

To achieve θ and sensitivity optimization, for different applied forces, the angle-resolved interrogation technique needs to scan a range of θ and then compare the angle-resolved power profile with that collected from the sensing fiber in an unloaded state.

Using smaller-diameter sensing fibers offer slight improvement to the detection limit or accuracy. This is because they result in larger N_r and lower stiffness that increases the sensitivity, but typically at the cost of coupling in less optical power, which reduces the signal-to-noise ratio.

Capillaries are attractive in that they deform more easily than fibers. However, not only do they offer poorer guidance of light, they also have shorter wall cavities for meridional rays than those for skew rays. The latter results in high-order meridional rays having the largest N_r below their critical angle. Hence, the localized rays lack coverage around the optical fiber. Increasing θ beyond their critical angle allow high-order skew rays to dominate, but with lower optical-power, lower SNR and thus higher detection-limit.

3. Experimental Setup

The first force sensor shown in Fig. 2(a) employs a straight POF (OMC OMPF1000) with core and cladding diameters of 980 ± 5 μm and 1000 ± 5 μm respectively. The material is Poly(methyl methacrylate) (PMMA) with a Young's modulus of 2.8–3.3 GPa, tensile yield strength of 64.8–83.4 MPa, and compressive yield strength of 110–124 MPa [24]. The POF is fixed across two steel

rods of 6000 $\pm$ 5 μm diameter (i.e., relatively large to avoid breaking the POF) and 60 $\pm$ 0.5 mm pitch with adhesives at the POF-rod and rod-surface contacts. The adhesives (Norland NOA-63) used have a Young's modulus of 1.65 GPa. Adhesives of higher Young's modulus can cause the adjacent fiber section to bend at larger angles, which elevates the risk of fiber breakage. However, such effect also increases the sensitivity. We chose NOA-63 for a good balance between these two attributes. The middle section of the POF ($\sim$60 mm) is pressed down by a force perpendicular to an aluminium base plate of 50 $\pm$ 0.5 mm width, and thus subject to force-induced bending. The distance between the two rods is limited by the minimum bend radius of the POF, below which it might break. The bent POF attenuates light via: (a) a gradual change in the fiber cross-section geometry over a relatively long fiber length, causing critical-angle breaches; and (b) a change in the refractive-index (RI) distribution in the POF, causing partial losses of optical guidance. To facilitate a balanced platform for different forces, an isolated strand of POF is also fixed in parallel between the two rods. The total length of the sensing POF is 2.5 $\pm$ 0.05 m and the fiber numerical-aperture is specified as 0.5. A comprehensive experimental study and/or a theoretical study is beyond the scope of this work.

The second force sensor shown in Fig. 2(b) was constructed in a similar fashion to the first, except two steel rods of 4000 $\pm$ 5 μm diameter (i.e., smaller to impart higher pressure at selective points) are spaced closer together at 50 $\pm$ 0.5 mm, and thus the aluminium base plate of 100 mm length compresses the free POF against the top surface of two steel rods. The distance between the two rods can be shortened. The compressed POF attenuates light via: (a) an abrupt change in the fiber cross-section geometry over a relatively short fiber length, causing deflection of some rays; and (b) a change in the RI distribution in the POF, causing a partial loss of optical guidance. This design aims to minimize the higher attenuation experienced by skew rays. Similarly, a disconnected POF is used for balance. The same lengths of POF are used as before.

Fig. 2(c) shows the schematic of the experimental setup used for both force sensors. To excite the POF, an unpolarized single-mode He-Ne laser source (Thorlabs HNLS008R-EC) was used. For suppressing laser intensity noise, a self-referencing was employed, where the laser beam was sampled with a 10° tilted glass wedge. The optical power of the sampled laser beam monitored with a reference commercial power meter (Thorlabs S120C, PM100D) will be used later to rescale the transmitted optical power. To provide a Gaussian intensity distribution, the collimated beam excited the POF with a spot diameter larger than the cladding diameter of the POF (i.e., 3:1 ratio). For meridional rays, s-polarized light at the fiber end-face leads to a higher transmission than that of p-polarized light. It is the opposite for high-order skew rays. Hence, to support the transmission of both meridional rays and skew rays, unpolarized light was used. To ensure a consistent input optical power, the flat-cleaved input end of the POF was mounted on a motorized rotation stage (Thorlabs CR1/M-Z7) such that the end-face was positioned at the center of rotation. Owing to the slack and slightly straight arrangement of the POF, rotations do not create sufficiently large bend angles to cause noticeable power modulations in the transmitted light. To deliver the maximum optical power for increasing the signal-to-noise ratio and thus decreasing the detection limit or accuracy, the collimated beam was centered on the fiber. The light entering the POF from it sides mostly leaks out due to the refraction of light, and thus conversion into significantly higher-order rays that cannot be guided. Although skew rays can also be generated from focused light, the contribution from meridional rays and low-order skew rays limit the sensitivity and destabilizes the alignment. Light is guided only in the core, because the cladding is highly lossy from exposure to high-RI adhesive on the fiber mount.

For the first force sensor, a base plate was placed on the two POFs between the two rods. For the second force sensor, it was placed on the two POFs on top of the two rods. To collect the transmitted rays, an integrating sphere (Thorlabs S142C) with a power meter (Thorlabs PM100D) was used. To compensate for the reduced input optical power due to the Lambertian angle effect, a division by the cosine of θ was applied. No compensation is needed for the angle-dependent reflectivity, because its contribution within the range of interest of $\theta < 60$ deg is negligible (i.e., $<8\%$ Fresnel reflectivity). These effects produce a flat-top angle-resolved power profile, but do not affect the force-induced attenuation due to a cancelation of scaling.
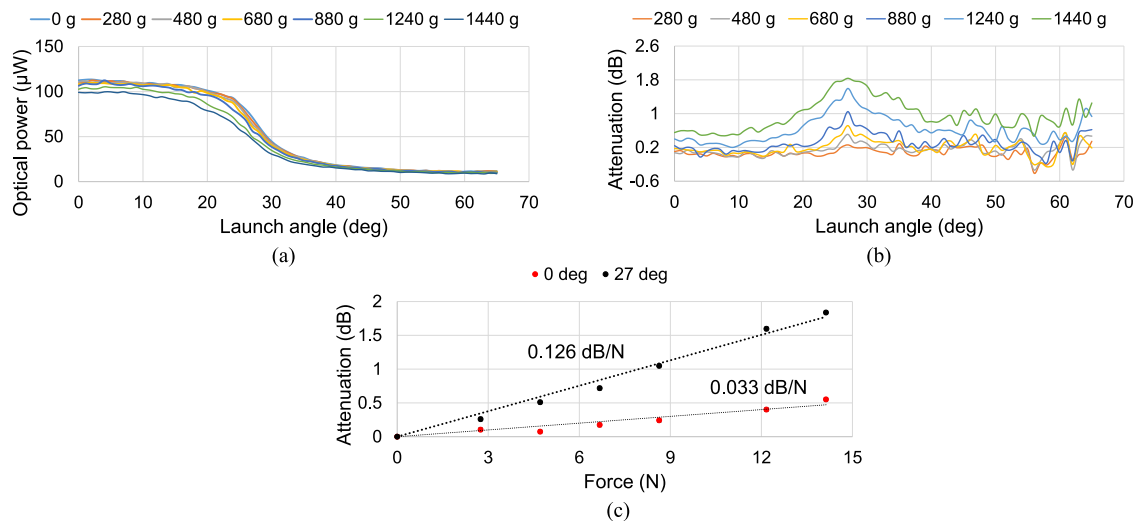
Fig. 3. First force sensor: (a) angle-resolved optical power for different masses; (b) angle-resolved attenuation for different masses; and (c) attenuation as a function of applied force for different launch angles, with linear fit and error bars.

4. Results and Discussion

The upper limit in the range of θ were chosen based on the minimum θ that results in a transmitted optical power close to the noise floor, or the minimum θ where no superior sensitivity enhancement is certain, whichever is smaller. For the first force sensor, the measured angle-resolved power profile for different masses is plotted in Fig. 3(a), and its attenuation relative to the zero-weight baseline is shown in Fig. 3(b). It is clear that the attenuation for all masses is at their maximum around $\theta = 27$ deg. This results from a constructive combination of the aforementioned changes in fiber cross-section geometry and RI distribution. The attenuation is less at lower θ, as anticipated since the fundamental mode in optical fibers is more resilient to bending [25]. The attenuation fluctuates at $\theta > 40$ deg, due the effects of low signal-to-noise ratio. The RH of the measurement environment varied between 40–60%RH without causing noticeable changes in the measured data.

By analyzing the dataset at $\theta = 0$ deg, the sensitivity shown in Fig. 3(c) is 0.033 dB/N, from taking the slope of the linear fit of the relationship between the force (i.e., weight = mass $\times$ g, where g = acceleration of gravity = 9.81 m/s^2) and the corresponding attenuation. For $\theta = 27$ deg, the sensitivity is much higher at 0.126 dB/N. The deviations from the linear fit were likely caused by the sensing mechanism rather than noise/errors. The enhancement factor of sensitivity is 3.8 over the default launch condition of $\theta = 0$ deg. Owing to the balanced platform, the local sensitivity for the sensing fiber is doubled at 0.252 dB/N. Virtually no hysteresis was observed for increasing or decreasing the applied force, which is in agreement with a study on polymer planar Bragg grating [26].

For a low-cost construction of the force sensor, a temperature-stabilized light-emitting diode can be glued to a graded-index lens, and an angle-cleaved POF or flat-cleaved POF at an angle.

The system noise measured over 10 min is 1.1 μW for a transmitted optical power of 333.5 μW. The attenuation errors due to system noise and measurement repeatability errors are 0.028 dB. The detection limit or accuracy is 222.2 mN, from dividing the attenuation error by the sensitivity of 0.126 dB/N. The corresponding error bars for attenuation and applied force ($\pm$49.1 mN) are plotted in Fig. 3. Although the demonstrated range of forces range from 222.2 mN to 14.1 N, limited by the strength of the adhesives, the actual dynamic range should be wider.

The temporal characteristics (10–90%) shown in Fig. 4(a) were measured by placing/removing a mass on the aluminium plate and recording the transmission of the POF set at $\theta = 27$ deg as a
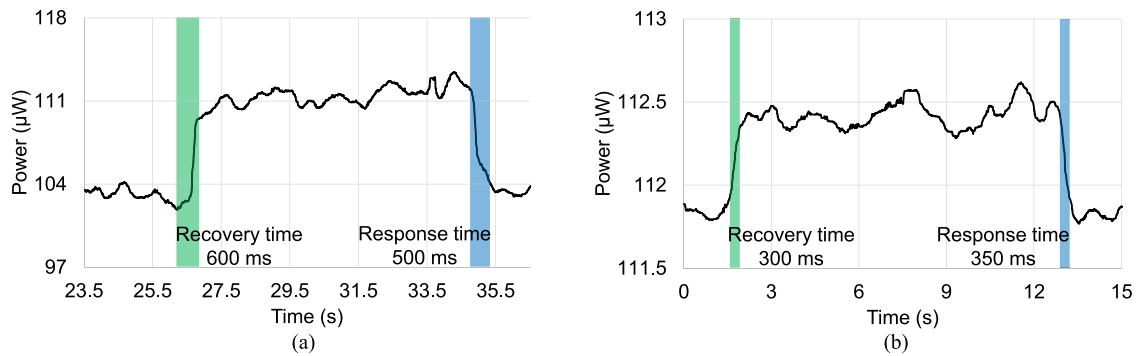
Fig. 4. Temporal characteristics of: (a) first force sensor; and (b) second force sensor; for a launch angle of 27 deg.
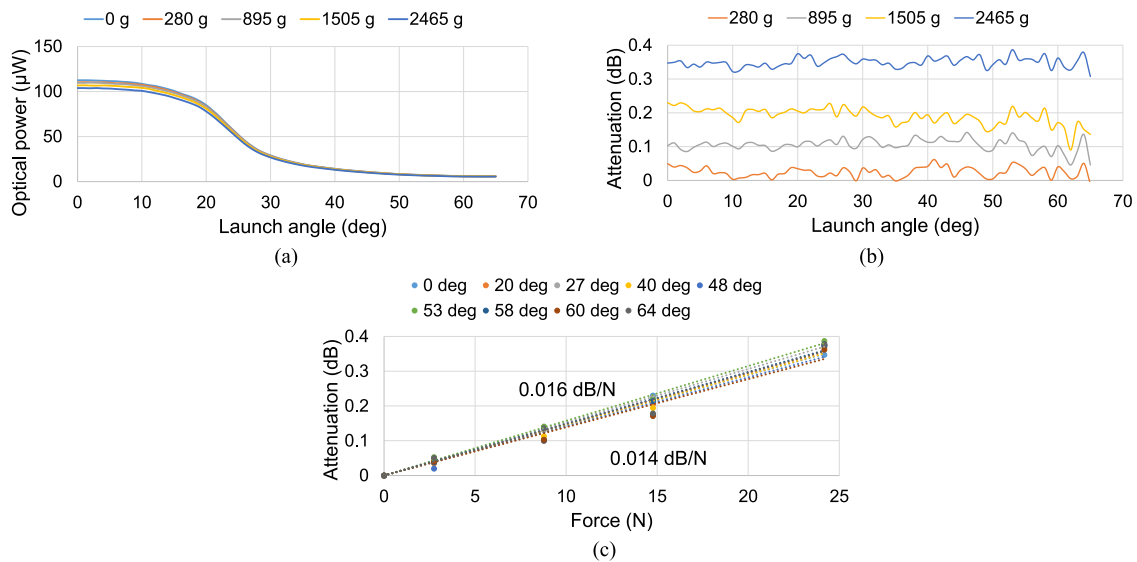

Fig. 5. Second force sensor: (a) angle-resolved optical power for different masses; (b) angle-resolved attenuation for different masses; and (c) attenuation as a function of applied force for different launch angles, with linear fit and error bars.

function of time. The response/recovery times were observed to be 500 ± 5 ms and 600 ± 5 ms respectively. Different masses achieved similar temporal characteristics.

For the second force sensor, the measured angle-resolved power profile for different masses is plotted in Fig. 5(a), and its attenuation relative to the zero-weight baseline is shown in Fig. 5(b). It is evident that the attenuation for all masses have no observable dependency on θ, which is attributed to a balance of the aforementioned changes in fiber cross-section geometry and RI distribution. The insensitivity to θ improves the fabrication tolerance of the force sensor, such that if the section of POF near the output of the laser source is relatively bend insensitive.

By analyzing the dataset between $\theta = 0$ deg and $\theta = 64$ deg, the relationship between force and attenuation is plotted in Fig. 5(c). The sensitivity is approximately linear between 0.014 dB/N and 0.016 dB/N. There is a small deviation of 6.7% of sensitivity centered at 0.015 dB/N with changes in θ. Within the range of tested forces (<25 N), θ deviations within 0–20 deg translates to negligible force errors. Owing to the balanced platform, the local sensitivity for the sensing fiber is doubled at 0.028–0.032 dB/N. The sensitivities are lower than those of the first force sensor, primarily because
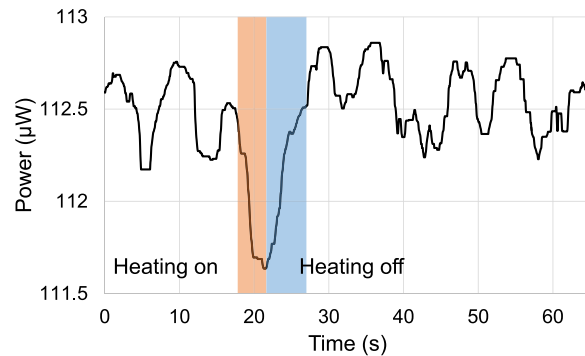
Fig. 6. Temporal response of the impact of heating/cooling on the first force sensor.

optical fibers are less sensitive to transverse compression than longitudinal bending. Similarly, no noticeable hysteresis was observed.

For both force sensors, their sensitivities can be improved by optimizing the geometry, and using a fiber material with a lower Young's modulus (e.g., 1.2 GPa with annealed dye-doped PMMA [27], 90 kPa with liquid-metal micro-droplets-infused elastomer [28]). Their dynamic ranges can be increased by choosing a fiber material with a higher tensile yield strength or a higher compressive yield strength.

The attenuation errors were found to be 0.014 dB, which is half of that of the first force sensor. The detection limit or accuracy is 875.0 mN, from dividing the noise equivalent attenuation by the sensitivity of 0.016 dB/N. The corresponding error bars for attenuation and applied force ($\pm$49.1 mN) are plotted in Fig. 5. Although the tested range of forces range from 875.0 mN to 24.2 N, the true dynamic range is expected to be broader.

Owing to the properties of PMMA, both force sensors are inherently cross-sensitive to temperature and vibrations, which could limit the type of measurement environments. Mechanical vibrations in industrial environments tend to produce repetitive signals with fixed frequencies, which can be filtered via signal processing. An ambient temperature drift from 23 °C to 35 °C created with a hot-air gun and measured with a reference thermocouple resulted in a change of <0.033 dB shown in Fig. 6. Since these two forces sensors are designed to work around room temperature (21–23 °C), their sensitivities and temporal characteristics were not investigated. It is anticipated that the performances will change with temperature, due to the dynamics of the polymer chains under different thermal conditions [29].

The response/recovery times shown in Fig. 4(b) were observed to be 350 $\pm$ 5 ms, and 300 $\pm$ 5 ms respectively. Fluctuations are caused by ambient temperature drifts, but it is still possible to determine the temporal characteristics via the polarity reversal in power change. Different masses achieved similar temporal characteristics. The second force sensor is faster than the first, because the stress inside the sensing fiber covers a smaller volume, and thus the relaxation time is shorter.

5. Conclusion

We have shown a bend-loss-based force sensor in which pure skew rays can enhance its sensitivity by a factor of 3.8 over the mixture of rays created from normal incidence to enable a sensitivity of 0.126 dB/N. Its dynamic range was tested from 222.2 mN to >14.1 N. The response/recovery times were measured to be 500 ms and 600 ms respectively. In addition, we demonstrated a compression-loss-based force sensor exhibiting a small deviation of 6.7% in sensitivity of 0.015 dB/N against changes in the launch angle of light. Its dynamic range was measured from 875.0 mN to >24.2 N. The response/recovery times were observed as 350 ms and 300 ms respectively. Their sensitivities and dynamic ranges can be improved by optimizing the geometry, and using a fiber material with a lower Young's modulus such as annealed dye-doped PMMA or a liquid-metal micro-droplets-infused

elastomer. The technique of using skew rays to enhance the sensitivity could be extended to other designs of force sensors based on optical fibers.

Acknowledgment

References

[1] A. M. Almassri *et al.*, "Pressure sensor: State of the art, design, and application for robotic hand," *J. Sens.*, vol. 2015, 2015, Art. no. 846487.
[2] C. Lopatin, "Aerospace applications of optical fiber mechanical sensors," in *Opto-Mechanical Fiber Optic Sensors*, H. Alemohammad Ed. New York, NY, USA: Elsevier, 2018.
[3] M. Krehel, R. M. Rossi, G. Bona, and L. J. Scherer, "Characterization of flexible copolymer optical fibers for force sensing applications," *Sensors*, vol. 13, no. 9, pp. 11956–11968, 2013.
[4] R. Khamimatul Ula and D. Hanto, "Performance weight sensor using graded index optical fiber on static test with UTM," *J. Phys.*, vol. 853, 2017, Art. no. 012016.
[5] X. Hu *et al.*, "Polarization effects in polymer FBGs: Study and use for transverse force sensing," *Opt. Exp.*, vol. 23, no. 4, pp. 4581–4590, 2015.
[6] L. Xu, L. A. Feuerman, J. Ge, K. R. Nilsson, and M. P. Fok, "Temperature-insensitive contact force sensing in bi-directional catheter using fiber Bragg grating pair," *IEEE Sensors J.*, vol. 17, no. 16, pp. 5118–5122, Aug. 2017.
[7] J. C. Vieira, O. M. F. Morais, C. M. A. Vasques, and R. de Oliveira, "A laboratorial prototype of a weight measuring system using optical fiber Bragg grating sensors embedded in silicone rubber," *Measurement*, vol. 61, pp. 58–66, 2015.
[8] F. Jiménez *et al.*, "Analysis of a plastic optical fiber-based displacement sensor," *Appl. Opt.*, vol. 46, no. 25, pp. 6256–6262, 2007.
[9] A. Vijayan, S. Gawli, A. Kulkarni, R. N. Karekar, and R. C. Aiyer, "An optical fiber weighing sensor based on bending," *Meas. Sci. Technol.*, vol. 19, no. 10, 2008, Art. no. 105302.
[10] P. Kumar, S. K. Singh, and P. Ojha, "Bifurcated optical fiber sensor for weight measurement system," in *Proc. Int. Conf. Comput. Intell. Commun. Syst.*, Gwalior, India, 2011, Art. no. 12461674.
[11] Y. Gong *et al.*, "Highly sensitive force sensor based on optical microfiber asymmetrical Fabry–Perot interferometer," *Opt. Exp.*, vol. 22, no. 3, pp. 3578–3584, 2014.
[12] S. Pirozzi, "Multi-point force sensor based on crossed optical fibers," *Sens. Actuators A, Phys.*, vol. 183, pp. 1–10, 2012.
[13] G. Liu and S. L. Chuang, "Polarimetric optical fiber weight sensor," *Sens. Actuators A, Phys.*, vol. 69, pp. 143–147, 1998.
[14] K. Yu, C. Wu, M. Sun, C. Lu, H. Tam, and Y. Zhao, "Fiber laser sensor for simultaneously axial strain and transverse-load detection," *Measurement*, vol. 62, pp. 137–141, 2015.
[15] K. S. C. Kuang, S. T. Quek, C. G. Koh, W. J. Cantwell, and P. J. Scully, "Plastic optical fibre sensors for structural health monitoring: A review of recent progress," *J. Sens.*, vol. 2009, 2009, Art. no. 312053.
[16] A. Cozannet and M. Treheux, "Skew rays in optical fibers," *Appl. Opt.*, vol. 14, no. 6, pp. 1345–1350, 1975.
[17] G. Y. Chen, C. A. Codemard, and M. N. Zervas, "Enhanced pump absorption of active fiber components with skew rays," *J. Lightw. Technol.*, vol. 34, no. 24, pp. 5642–5650, 2016.
[18] M. Hashimoto, "Circularly polarized modal skew rays in graded-index optical fibers," *J. Opt. Soc. Amer.*, vol. 72, no. 9, pp. 1147–1151, 1982.
[19] A. Bekshaev and M. Vasnetsov, "Vortex flow of light: "Spin" and "Orbital" flows in a circularly polarized paraxial beam," in *Twist Photons: Applications of Light With Orbital Angular Momentum*, J. P. Torres and L. Torner Ed. New York, NY, USA: Wiley, 2011.
[20] G. Y. Chen *et al.*, "Enhanced responsivity with skew mode excitation of transmission- and reflection-type refractometric sensors," *Opt. Lett.*, vol. 39, no. 13, pp. 3822–3825, 2014.
[21] Y. S. Dwivedi, A. K. Sharma, and B. D. Gupta, "Influence of skew rays on the sensitivity and signal-to-noise ratio of a fiber-optic surface-plasmon-resonance sensor: A theoretical study," *Appl. Opt.*, vol. 46, no. 21, pp. 4563–4569, 2007.
[22] G. Y. Chen, D. Otten, Y. Q. Kang, T. M. Monro, and D. G. Lancaster, "Measuring the radial position of defects within optical fibers using skew rays," *J. Sens.*, vol. 2017, 2017, Art. no. 4879528.
[23] P. D. Lin and C. Tsai, "Skew ray tracing and sensitivity analysis of ellipsoidal optical boundary surfaces," *Appl. Math. Model.*, vol. 32, no. 12, pp. 2526–2537, 2008.
[24] MatWeb PMMA overview, 2018. [Online]. Available: http://www.matweb.com/search/datasheet.aspx?bassnum=O1303&ckck=1
[25] C. Schulze *et al.*, "Mode resolved bend loss in few-mode optical fibers," *Opt. Exp.*, vol. 21, no. 3, pp. 3170–3181, 2013.
[26] M. Rosenberger, S. Hessler, S. Belle, B. Schmauss, and R. Hellmann, "Compressive and tensile strain sensing using a polymer planar Bragg grating," *Opt. Exp.*, vol. 22, no. 5, pp. 5483–5490, 2014.
[27] C. Jiang, "Fabrication and mechanical behavior of dye-doped polymer optical fiber," *J. Appl. Phys.*, vol. 92, no. 1, pp. 4–12, 2002.
[28] M. D. Bartlett *et al.*, "High thermal conductivity in soft elastomers with elongated liquid metal inclusions," *PNAS*, vol. 114, no. 9, pp. 2143–2148, 2016.
[29] N. Jing, C. Teng, X. Zhao, and J. Zheng, "Temperature dependence of a refractive index sensor based on a macrobending micro-plastic optical fiber," *Appl. Opt.*, vol. 54, no. 8, pp. 1890–1893, 2015.